J. Fluid Mech. (2007), *vol.* 573, *pp.* 311–337.
doi:10.1017/S0022112006003922 Printed in the United Kingdom

Droplet–particle collision mechanics with film-boiling evaporation

YANG GE AND L.-S. FAN†

Department of Chemical and Biomolecular Engineering, The Ohio State University, Columbus, OH 43210, USA

(Received 8 July 2005 and in revised form 10 August 2006)

A three-dimensional numerical model is developed to simulate the process of collision between an evaporative droplet and a high-temperature particle. This phenomenon is of direct relevance to many engineering process operations, such as fluid catalytic cracking (FCC), polyethylene synthesis,and electronic materials coating. In this study, the level-set method and the immersed-boundary method are combined to describe the droplet–particle contact dynamics in a fixed Eulerian grid. The droplet deformation is captured by one level-set function while the solid–fluid boundary condition is imposed on the particle surface through the immersed-boundary method involving another level-set function. A two-dimensional vapour-layer model is developed to simulate the vapour flow dynamics. Equations for the heat transfer characteristics are formulated for each of the solid, liquid and gas phases. The incompressible flow-governing equations are solved using the finite-volume method with the ALE (arbitrary Lagrangian Eulerian) technique. The simulation results are validated through comparisons with experimental data obtained from the new experimental set-up designed in this study. An important feature of the droplet impacting on a particle with film boiling is that the droplet undergoes a spreading, recoiling and rebounding process, which is reproduced by the numerical simulation based on the model. Details of the collision such as spread factor, contact time and temperature distribution are provided. Simulations are also conducted to examine the effects of the particle size and the collision velocity. Although the value for the maximum spread factor is larger for a higher impact velocity and for a smaller particle, the contact time is independent of the impact velocity and particle size. Both the normal collision and the oblique collision are considered in this study.

1. Introduction

Many engineering process operations involve the collision of liquid droplets with solid particles at high temperatures. In the petroleum industry, a fluid catalytic cracking (FCC) riser with an evaporative liquid jet is designed to provide effective liquid–solid contact and hence an increased rate of catalytic reactions in the riser. In the riser reactor, liquid hydrocarbon at a low temperature is injected from feed nozzles located at the bottom of the reactor, and the droplets formed from the spray are in contact with high-temperature fluidized catalyst particles (Fan *et al.* 2001).

† Author to whom correspondence should be addressed.

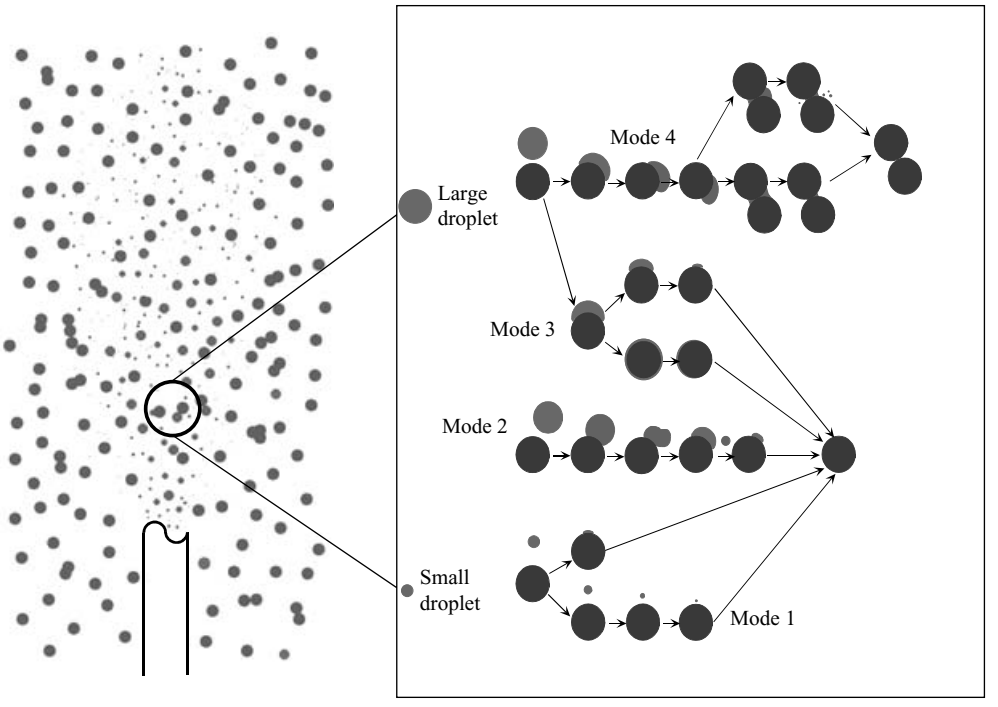

FIGURE 1. Various modes of droplet–particle collisions (Zhu *et al.* 2000).

The vaporized hydrocarbon then carries the catalyst particle up through the riser. In the feed nozzle region, the size of the formed droplets can be comparable to or significantly larger than the size of the particle. With the droplets and particles of different sizes having different momentum at contact, the collision of the particles and the droplets may experience different contact modes (figure 1) (Zhu, Wang & Fan 2000). Smaller droplets may rebound from the surface of a larger particle upon impact because of the nature of the non-wetting contact (Mode 1 in figure 1). A smaller particle may penetrate or be retained inside the larger droplet (Mode 3 in figure 1). Droplets may splash during the impact (Mode 2 in figure 1) or remain attached to the particle surface after the collision, thereby intensifying particle aggregation (Mode 4 in figure 1). Thus, understanding the droplet and particle contact mechanics is crucial to an accurate account of the momentum and heat transfer processes between the droplets and particles, and is important to the prediction of hydrocarbon product distributions in the light of catalytic or thermal cracking reactions in the riser.

The droplet–particle collision processes in feed nozzle conditions are always accompanied by intense evaporation. In an FCC riser reactor, since the temperature of the catalytic particle is much larger than the saturation temperature of the oil droplet, the hydrocarbon vapour generated from evaporation forms a thin vapour layer which may prevent direct contact between the droplet and the particle. Under this condition, the non-wetting contact may take place during the collision marking the film-boiling regime, or Leidenfrost regime (Gottfried, Lee & Bell 1966). A feature of the contact in the Leidenfrost regime is that the heat flux at the contact area is significantly smaller than that in the nucleate boiling regime and the transition-boiling regime, even though the temperature gradient across the vapour layer is higher. The vapour layer hinders the heat transfer from the solid to the droplet.

This study attempts to develop a three-dimensional model based on the level-set approach and the immersed boundary method to simulate the collision of a droplet with a superheated particle in the film-boiling condition. The free surface of the deformable droplet and the rigid surface of the solid particle are captured by two separate level-set functions in a fixed regular Eulerian grid. The immersed boundary method is applied to impose the solid–fluid boundary condition at the particle surface. The governing equations for the droplet and the surrounding gas phase are solved using the finite volume method with the ALE (arbitrary Lagrangian Eulerian) technique. A two-dimensional vapour-layer model is developed on a boundary-layer coordinate to simulate the vapour flow dynamics inside the micro-scale vapour layer between the droplet and the particle. The heat transfer equations for the gas phase and the particle phase are solved by considering the energy balance at the solid–vapour and vapour–liquid interfaces. Experiments are also conducted to substantiate the model and the simulation results based on the model obtained in this study.

2. Survey of previous studies

Extensive experiments were conducted to study the droplet impact on a flat surface under the film-boiling condition in the literature (e.g. Wachters & Westerling 1966; Inada, Miyasaka & Nishida 1985; Chandra & Avedisian 1991; Hatta *et al.* 1997). The Weber number, defined by $We = \rho U_0^2 d_0/\sigma$, was found to be able to characterize the droplet collision dynamics (Wachters & Westerling 1966). The Leidenfrost temperature was determined as the temperature when the non-wetting contact occurs as the surface temperature increases (Chandra & Avedisian 1991). The hydrocarbon droplet (*n*-heptane) was found to have a much lower transition temperature than the water droplet (Qiao & Chandra 1996). When the surface temperature is above the Leidenfrost temperature of the liquid, the dynamics of the droplet were found to be independent of the surface materials (Hatta *et al.* 1997). The effects of the initial droplet temperature, which characterizes the subcooling degree of the droplet, on the behaviour of the film-boiling impact were also reported (Inada *et al.* 1985; Chen & Hsu 1995; Ge & Fan 2006).

Numerical simulations were performed to describe the droplet impingement on an isothermal flat wall (e.g. Harlow & Shannon 1967; Fukai *et al.* 1995; Pasandideh-Fard *et al.* 1998; Bussmann, Mostaghimi & Chandra 1999, 2000; Zheng & Zhang 2000; Francois & Shyy 2003; Mehdi-Nejad, Mostaghimi & Chandra 2003). In these simulations, the numerical techniques used to solve the moving-interface problem generally related to two basic methods: the front-tracking method and the front-capturing method. The front-tracking method includes the adaptive-grid finite-element method (Fukai *et al.* 1995) and the immerse boundary method (IBM) (Francois & Shyy 2003). In the front-tracking method, the interface is explicitly described by a discrete set of markers or by a set of deformable structured mesh points. The interface motion is tracked by the advection of the Lagrangian markers in a flow field. The front-capturing method, on the other hand, includes the volume of fluid (VOF) method (Pasandideh-Fard *et al.* 1998; Bussmann *et al.* 1999) and the level-set method (Zheng & Zhang 2000). In the front-capturing method, the moving front is implicitly represented by a scalar function defined on Eulerian mesh points. The advection equation of a scalar function, which is the fluid volume fraction (VOF method) or the level–set function (level-set method), is solved to trace the interface movement. The interface force such as the surface tension force is incorporated in the

flow momentum equation as a source term using the continuum surface force (CSF) method (Brackbill, Kothe & Zemach 1992).

The front-capturing method was coupled with the heat transfer model to solve the problem involving the droplet impact on a superheated flat surface with evaporation (Karl *et al.* 1996; Fujimoto & Hatta 1996; Harvie & Fletcher 2001*a*, *b*; Chizhov & Takayama 2004; Ge & Fan 2005). A two-dimensional Marker-and-Cell (MAC) type solution method was used by Fujimoto & Hatta (1996) and an alternative no-slip and free-slip boundary condition was applied to the solid surface in the droplet spreading and recoiling stages. Karl *et al.* (1996) applied a free-slip boundary condition and employed a contact angle of 180° on the solid surface to simulate the impact of small ethanol droplets (100–200 μm) on the wall in the superheating condition. The two-dimensional VOF method was used to account for the rebound of the droplet from the surface. Harvie & Fletcher (2001*a*, *b*) combined a two-dimensional VOF algorithm with a one-dimensional axisymmetric vapour flow model to simulate the liquid droplet evaporation from a hot solid surface. Ge & Fan (2005) developed a three-dimensional numerical model based on the level-set method and finite-volume technique to simulate the saturated droplet impact on a superheated flat surface. A two-dimensional vapour flow model was coupled with the heat transfer model to account for the vapour flow dynamics induced by the Leidenfrost evaporation. This model was also extended to predict the subcooled droplet impact in which the initial temperature of the droplet is lower than the saturated temperatures of the liquid (Ge & Fan 2006). The transient heat transfer behaviour inside the droplet and the solid was calculated with the kinetic slip treatment applied to the boundary condition at the liquid–vapour and vapour–solid interface, which modified the continuum boundary relationship. The predicted droplet dynamics and the heat transfer rate at the surface from this model matched well with the experimental data reported in the literature.

The theoretical description of the process of evaporative liquid droplets in collision with high-temperature particles is difficult owing to the complex interplay among hydrodynamic and thermodynamic factors, such as deformable interface, moving solid boundary, heat transfer and phase changes. Little has been reported in the literature concerning such a description. In the numerical analysis, the droplet and particle surface movement in the flow field must be accurately simulated with the flow boundary condition at the particle surface to be satisfied. As the axisymmetric normal collision represents only one of many possible droplet–particle contact scenarios, a three-dimensional simulation accounting for the oblique collision is necessary. Also, the heat transfer resistance and the micro-scale hindering force induced by the vapour layer from liquid evaporation must be considered in the simulation model.

3. Experimental methodology

The schematic diagram of the experimental set-up is shown in figure 2. The main experimental apparatus consists of a syringe, blunt-point needles of 17 gauge, 21 gauge and 27 gauge (corresponding to 1.067, 0.495 and 0.191 mm nominal inner diameter, respectively), and brass solid particles of sizes 5.5 mm and 3.2 mm. The brass particle is heated on a heating plate with adjustable temperature settings. The syringe is covered with two layers of insulation to prevent external heating of the liquid from the plate heater. The initial droplet and the surrounding atmospheric air are at room temperature. A high-speed camera capable of capturing 500 frames per second is used to record the droplet–particle collision process. Two light sources are used to illuminate the particle and droplet from both the front and the back. A

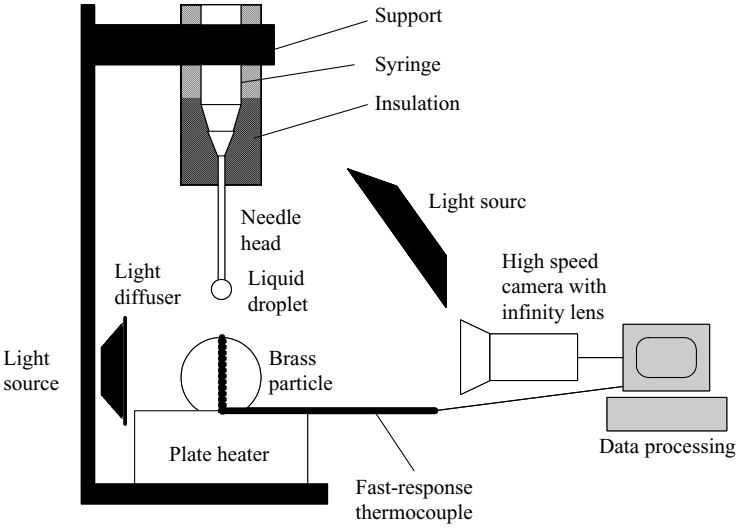

FIGURE 2. A schematic diagram of the experimental set-up.

light diffuser is placed in front of the backlight source to provide soft background lighting. A small hole is drilled along the axis of the brass particle. A state-of-the-art fast-response type T thermocouple constructed from 0.15 mm mineral insulated cable is inserted from the bottom and through the centre of the particle to the particle surface. The thermocouple tip is flush mounted with the particle surface. A separate experiment was conducted to substantiate the thermocouple response time by exposing the thermocouple set-up in boiling water at 100 °C. This experiment reveals a response time on average of ∼2.0 ms. The fast response time for the thermocouple is crucial to the measurement of the rapid temperature change on the particle surface, which is at a time scale of ∼10 ms, during the collision process. Different sizes of droplets are formed by different needle sizes of the syringe. Small droplets can also be formed with the aid of acoustic forces. By changing the height of the syringe, a wide range of Weber number for both the normal and oblique collisions can be established.

Based on the video frames, the droplet–particle contact area and the droplet height relative to the particle are measured.

4. Mathematical model and numerical method

In this study, we developed a numerical model to describe the unsteady three-dimensional fluid-flow phenomena for the droplet impact on a particle surface with evaporation. This model is built on the level-set method (Osher & Sethian 1988) and immersed boundary method (Peskin 1977) to address effectively the three-dimensional droplet deformation and the solid-boundary problems at the particle surface with a fixed Cartesian mesh. In this model, two level-set functions are defined to represent the droplet interface (ϕ_d) and the moving particle surface (ϕ_p). The evaporation effect is accounted for by the vapour pressure force, which is calculated in a dynamic vapour flow model. The energy balance equations in each phase are solved with interface boundary conditions to yield the temperature distribution and the evaporation rate.

4.1. *Level-set method for capturing droplet surface*

The droplet free surface is taken as the zero in the droplet level-set function $\phi_d(\boldsymbol{x}, t)$, which is defined as:

$$\left.\begin{array}{l}\phi_d(\boldsymbol{x}, t) > 0 \text{ for } \boldsymbol{x} \text{ outside droplet,}\\ \phi_d(\boldsymbol{x}, t) < 0 \text{ for } \boldsymbol{x} \text{ inside droplet,}\\ \phi_d(\boldsymbol{x}, t) = 0 \text{ for } \boldsymbol{x} \text{ at interface.}\end{array}\right\} \tag{1}$$

The advection equation given below for the droplet level-set function (ϕ_d) is solved to capture the motion of the droplet surface.

$$\frac{\partial \phi_d}{\partial t} + \boldsymbol{V}_\Gamma \cdot \nabla \phi_d = 0, \tag{2}$$

where $\boldsymbol{V}_\Gamma$ is the velocity on the interface and t is time. Based on the experimental results of Wachters & Westerling (1966) on droplet impact, the mass loss of the droplet due to evaporation during a short contact process is negligibly small (<0.5 % of the total droplet mass). After updating the droplet level-set function (ϕ_d) at each time step using (2), an iterative re-distancing procedure is performed to set the level-set function to be equal to the distance function and to maintain the mass conservation of the droplet (Sussman *et al.* 1998).

With the droplet surface described by the level-set function, the computational domain is treated as a single fluid in a Eulerian frame and the density and viscosity of the flow are defined as:

$$\rho = \rho_l + H(\phi_d)(\rho_g - \rho_l), \tag{3}$$

$$\mu = \mu_l + H(\phi_d)(\mu_g - \mu_l), \tag{4}$$

where ρ_l and ρ_g are the density of the liquid and gas, respectively; and μ_l and μ_g are the viscosity of the liquid and gas, respectively. $H(\phi)$ is a smoothed Heaviside function and is defined as (Chen & Fan 2004):

$$H(\phi) = \begin{cases} 0 & \text{if } \phi \leqslant -\varepsilon, \\ \dfrac{\phi + \varepsilon}{2\varepsilon} + \dfrac{\sin(\pi\phi/\varepsilon)}{2\pi} & \text{if } |\phi| \leqslant \varepsilon, \\ 1 & \text{if } \phi \geqslant \varepsilon, \end{cases} \tag{5}$$

where ε is the thickness of the interface, which is a distance value relative to the grid space.

In the simulation, both liquid and gas phases are treated as incompressible. The equations of conservation of mass and momentum for this three-phase flow system can be given by:

$$\nabla \cdot \boldsymbol{V} = 0, \tag{6}$$

$$\rho\left(\frac{\partial \boldsymbol{V}}{\partial t} + \nabla \cdot \boldsymbol{V}\boldsymbol{V}\right) = -\nabla p + \rho \boldsymbol{g} + \nabla \cdot (2\mu \boldsymbol{D}) + \sigma\kappa(\phi_d)\delta(\phi_d)\nabla\phi_d + \boldsymbol{F}_p(\phi_p) + \boldsymbol{F}_{vapour}, \tag{7}$$

where $\boldsymbol{V}$ is the fluid velocity; $\rho = \rho(\phi_d)$ is the fluid density defined by (3); $\mu = \mu(\phi_d)$ is the fluid viscosity defined by (4); g is the acceleration due to gravity σ is the surface tension coefficient; and $\boldsymbol{D}$ is the rate of deformation tensor. The surface tension force is included in this model as a body force using the continuum surface model (CSM) (Brackbill *et al.* 1992). $\delta(\phi_d)$ is the one-dimensional delta function and $\kappa(\phi_d)$ is the

curvature of the free surface defined as (Sussman *et al.* 1998):

$$\kappa(\phi_d) = \nabla \cdot \frac{\nabla \phi_d}{|\nabla \phi d|}. \tag{8}$$

The CFDLIB code is used to solve the hydrodynamic equations. An explicit time-marching, cell-centred ICE (implicit continuous-fluid Eulerian) numerical technique is employed to solve the governing equations (equations (6)–(7)) (Kashiwa *et al.* 1994). The computation cycle is split into two distinct phases: a Lagrangian phase and a remapping phase, in which the ALE (arbitrary Lagrangian Eulerian) technique is applied to support the arbitrary mesh motion with fluid flow. If $\phi_d^n = \phi_d(\boldsymbol{x}, t^n)$ and $\boldsymbol{V}^n = \boldsymbol{V}(\boldsymbol{x}, t^n)$ are the cell-centred level-set function and the velocity at time t^n, respectively, the numerical procedures to solve $\boldsymbol{V}^{n+1}$ and ϕ_d^{n+1} at $t^{n+1} = t^n + \Delta t$ are described below.

1. Compute the velocity field $\boldsymbol{V}^{n+1}$ by solving the governing equations (6) and (7), using the cell-centred ICE technique and ALE technique (Kashiwa *et al.* 1994).

2. Solve for the convection equation of $\phi_d(\boldsymbol{x}, t)$ (equation (2)) to obtain $\bar{\phi}^{n+1}$. The high-order (third-order) ENO (essentially non-oscillatory) scheme is used to calculate the convective term $\boldsymbol{V}_\Gamma \cdot \nabla \phi$ based on the updated velocity field $\boldsymbol{V}^{n+1}$. The time advance is accomplished using the second-order TVD (total variation diminishing) Runge–Kutta method (Sussman *et al.* 1998).

3. Perform the redistance procedure to obtain the ϕ^{n+1} using $\bar{\phi}^{n+1}$ as the initial value (Sussman *et al.* 1998).

4. Calculate the density and the viscosity of the field using equations (3)–(5) with the updated level-set function ϕ^{n+1}.

In (7), the presence of the solid particle in the fluid is represented by a virtual boundary body force field, $\boldsymbol{F}_p(\phi_p)$, defined by the immersed boundary method, as discussed in § 4.2. $\boldsymbol{F}_{vapour}$ is vapour pressure force exerted on the droplet–particle contact area owing to the effect of evaporation, as discussed in § 4.3.

4.2. *Immersed-boundary/level-set method for particle–flow interaction*

The particle level-set function (ϕ_p) is defined as the signed distance from any given point $\boldsymbol{x}$ in the Eulerian system to the particle surface:

$$\phi_p = |\boldsymbol{x} - \boldsymbol{x}_o(t)| - R_p, \tag{9}$$

where $\boldsymbol{x}_0(t)$ is the position vector of the centre of the particle and R_p is the particle radius. With this definition, $\phi_p > 0$ when $\boldsymbol{x}$ is outside the particle, $\phi_p < 0$ when $\boldsymbol{x}$ is inside the particle.

The immersed boundary (IB) method was originally reported by Peskin (1977) to simulate the fluid flow in a complex geometrical configuration using a fixed Cartesian mesh. The basic idea of the immersed boundary method is that the presence of the solid boundary (fixed or moving) in a fluid can be represented by a virtual body force field $\boldsymbol{F}_p(\phi_p)$ applied on the computational grid at the vicinity of the solid–flow interface. It is noted that the virtual body force $\boldsymbol{F}_p(\phi_p)$ depends not only on the unsteady fluid velocity, but also on the velocity and location of the particle surface, which are also functions of time. There are several ways to specify this boundary force, such as the feedback forcing scheme (Goldstein, Handler & Sirovich 1993) and the direct forcing scheme (Fadlun *et al.* 2000). Considering the stability and efficiency in three-dimensional simulation, the direct forcing scheme is adopted in this model. In this scheme, the discretized momentum equation for the computational volume on

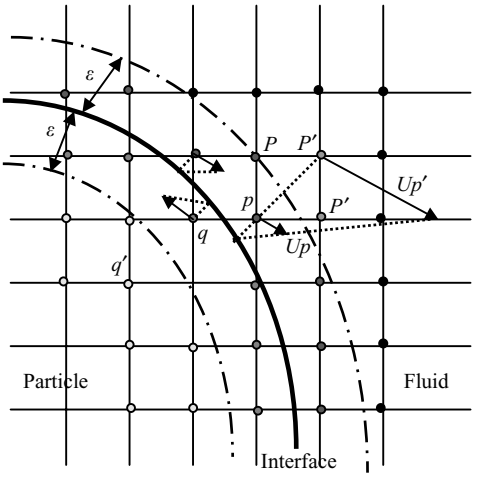

FIGURE 3. The velocity interpolation scheme based on the particle level-set function (no-slip).

the boundary is given as:

$$V^{t+1} = V^t + \Delta t\left(RHS^t + F_p^t\right), \tag{10}$$

where RHS refers to all the terms in the right-hand side of (7), except the virtual body force $\boldsymbol{F}_p(\phi_p)$ and vapour pressure force $\boldsymbol{F}_{vapour}$, divided by fluid density ρ. The effects of the virtual body force are to maintain the fluid velocity to satisfy the boundary condition at the particle surface. For a free-slip boundary condition, that is:

$$V^{t+1} = U_p(t)\cdot\boldsymbol{n} \tag{11}$$

where U_p is the particle velocity and $\boldsymbol{n}$ is the normal direction of particle surface. Thus, the discrete virtual force can be defined as:

$$F_p^t = (U_p\cdot\boldsymbol{n} - V^t)/\Delta t - RHS^t. \tag{12}$$

The computational grids are generally not coincident with the location of the particle surface. Therefore, it is most unlikely to have the surface for $\phi_p = 0$ located at a grid point. A velocity interpolation procedure must be carried out in order to calculate the boundary force and to apply this force to the control volume close to the immersed particle surface (Fadlun *et al.* 2000). In this study, a new interpolation scheme is developed, based on the particle level-set function (ϕ_p). The scheme as shown in figure 3 is described below.

During each time step of the simulation, the fluid–particle immersed boundary condition is imposed on the computational cells located in a small band across the particle surface (shown in figure 3). The thickness of this band (2ε) can be chosen to be equal to 3Δ, where Δ is the mesh size for a uniform mesh. For a grid point (p or q in figure 3), where the velocity components of the control volume are defined, located in this band, that is:

$$\varepsilon > \phi_p > -\varepsilon. \tag{13}$$

The velocity at this grid point is to be redefined using linear interpolation based on the velocity and particle level-set function (ϕ_p) at the neighbouring grid point (p'). For grid point p in figure 3, located in this band but outside the particle, the fluid

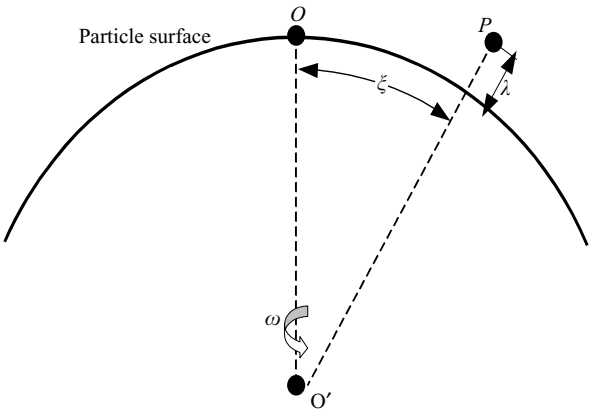

FIGURE 4. Boundary-layer coordinates.

velocity (V) at p is determined by (for no-slip boundary condition):

$$V_p = U_p(t) + \frac{\phi_p}{n}\sum_{i}^{n}\frac{V_{p',i} - U_p(t)}{\phi_{p',i}}, \tag{14}$$

where $V_{p'}$ and $\phi_{p'}$ are the velocity and particle level-set function, respectively, at the p' (in figure 3). The term n is the total number of neighbouring points. It should be noted that only the neighbouring grid points located outside the band are chosen to interpolate the velocity at point p. The velocities at these points (p') are obtained by solving the Navier–Stokes equation in the same manner as those far away from the interface. It can be seen that when $\phi_p = 0$, i.e. the grid point p is right on the particle surface, the velocity at p is equal to the particle velocity: $V_p = U_p(t)$.

The velocity at grid point q, which is located inside the small band (2ε) and inside the particle (figure 3), is determined by the neighbouring grid point outside the particle:

$$V_q = U_p(t) + \frac{\phi_q}{m}\sum_{i}^{m}\frac{V_{p,i} - U_p(t)}{\phi_{p,i}}, \tag{15}$$

where m is the total number of the neighbouring grid points which are located outside the particle.

4.3. *Vapour layer model*

For the film boiling impact simulation, a microscale vapour-layer model is required to determine the evaporation-induced pressure force $\boldsymbol{F}_{vapour}$ on both the droplet side and the moving particle side. Ge & Fan (2005) developed a two-dimensional model to simulate the dynamics of the vapour flow between the droplet and the flat surface considering the inertial force of the vapour. In this study, this model is extended to simulate the vapour flow within the particle–droplet contact area.

As the vapour flows along the spherical surface of the particle, a boundary-layer coordinate (ξ, λ, ω) (figure 4) is employed to describe the vapour-layer equation. In this coordinate, the Navier–Stokes equations for incompressible vapour flows with gravitation terms neglected are given by:

$$\frac{\partial u_\xi}{\partial \xi} + \frac{\cot(\xi/R)}{R}u_\xi + \frac{2}{R}u_\lambda + \frac{\partial u_\lambda}{\partial \lambda} = 0, \tag{16}$$

$$u_\xi \frac{\partial u_\xi}{\partial \xi} + u_\lambda \frac{\partial u_\xi}{\partial \lambda} + \frac{u_\xi u_\lambda}{R} = -\frac{\partial}{\partial \xi}\left(\frac{P}{\rho}\right) - \nu\left(\frac{\partial^2 u_\lambda}{\partial \xi \partial \lambda} - \frac{2}{R}\frac{\partial u_\xi}{\partial \lambda} - \frac{\partial^2 u_\xi}{\partial \lambda^2}\right), \tag{17}$$

$$u_\xi \frac{\partial u_\lambda}{\partial \xi} + u_\lambda \frac{\partial u_\lambda}{\partial \lambda} - \frac{u_\xi^2}{R} = -\frac{\partial}{\partial \lambda}\left(\frac{P}{\rho}\right) + \frac{\nu}{R}\left[R\frac{\partial^2 u_\lambda}{\partial \xi^2} - \frac{\partial u_\xi}{\partial \xi} - R\frac{\partial^2 u_\xi}{\partial \xi \partial \lambda} + \cot\left(\frac{\xi}{R}\right)\left(\frac{\partial u_\lambda}{\partial \xi} - \frac{u_\xi}{R} - \frac{\partial u_\xi}{\partial \lambda}\right)\right], \tag{18}$$

where u_ξ, u_λ are the vapour flow velocities in the ξ and λ directions, respectively.

Considering that the thickness of the vapour layer ($\sim\mu$m) is much smaller than the radius of the droplet and the particle ($\sim$mm), the momentum equations of the vapour flow can be simplified based on the order of magnitude analysis as given by:

$$u_\xi \frac{\partial u_\xi}{\partial \xi} + u_\lambda \frac{\partial u_\xi}{\partial \lambda} = -\frac{\partial}{\partial \xi}\left(\frac{P}{\rho}\right) + \nu\frac{\partial^2 u_\xi}{\partial \lambda^2}, \tag{19}$$

$$\frac{\partial}{\partial \lambda}\left(\frac{P}{\rho}\right) = 0. \tag{20}$$

The boundary conditions are:

$$\left.\begin{aligned} &\lambda = 0,\ u_\xi(\xi, 0) = u_\lambda(\xi, 0) = 0, \\ &\lambda = \delta,\ u_\xi(\xi, \delta) = u_l(\xi), u_\lambda(\xi, \delta) = u_{\lambda\delta}(\xi), \\ &\xi = 0, \frac{\partial}{\partial \xi} = 0; \xi = \xi_b, p = p_b, \end{aligned}\right\} \tag{21}$$

where $u_l(\xi)$ is the droplet surface velocity in the ξ-direction; δ is the vapour-layer thickness; $u_{\lambda\delta}(\xi)$ is the local vapour velocity; ξ_b is the radius of the extent of the contact area; p_b is the pressure of the ambient gas at the outside edge of the vapour layer.

The inertial force of the vapour flow in the film boiling condition is of the same order of magnitude as the viscous force and cannot be neglected. A variable transformation is considered to solve (19) and (20):

$$\left.\begin{aligned} u_\lambda(\xi, \eta) &= -\eta\ u_{\lambda\delta}(\xi), \\ u_\xi(\xi, \eta) &= \Omega(\xi)\ \Phi(\eta), \end{aligned}\right\} \tag{22}$$

where $\eta = \lambda/\delta$. The value of $u_{\lambda\delta}(\xi)$ can be calculated through the energy balance equation at the vapour–droplet interface, as discussed in §4.4. The functions $\Omega(\xi)$ and $\Phi(\eta)$ are single variables. With this transformation, the ξ momentum equation can be converted to an ordinary differential equation (ODE). Under the condition that the evaporation Reynolds number $Re_\delta = \delta(\xi)u_{\lambda\delta}/\nu \leqslant O(1)$, $\Phi(\eta)$ can be approximated by including the first three terms in the power series of the general solution of the ODE:

$$\Phi(\eta) = \Phi_\delta \eta - \varphi(\xi)\eta\left(\frac{1}{2} - \frac{Re_\delta}{24}\right) + \varphi(x)\left(\frac{\eta^2}{2} - \frac{Re_\delta}{24}\eta^4\right). \tag{23}$$

Thus, the vapour pressure distribution can be determined by:

$$p(\xi) = p_b + \int_\xi^{\xi_b} \rho\varphi(\xi')\,\mathrm{d}\xi', \tag{24}$$

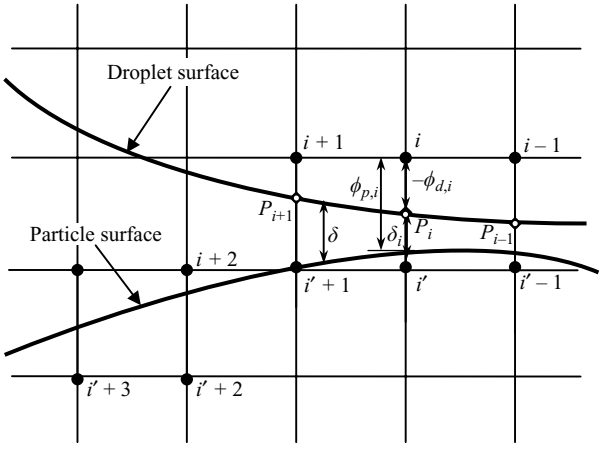

FIGURE 5. The schematic diagram for determining the thickness of the vapour layer.

and $\varphi(\xi)$ is given by:

$$\varphi(\xi) = \frac{12\gamma}{\delta^2\left(1 - \frac{3}{20}Re_\delta\right)}\left(\bar{u}_\xi(\xi) - \tfrac{1}{2}u_{l\delta}(\xi)\right). \tag{25}$$

The averaged velocity of the vapour can be expressed based on the continuity equation as:

$$\bar{u}_\xi(\xi) = \frac{1}{\xi\,\delta(\xi)}\int_0^\xi \xi' u_{\lambda\delta}(\xi')\,\mathrm{d}\xi'. \tag{26}$$

At each time step, equations (24)–(26) are solved using the piecewise integration method to obtain the averaged vapour flow velocity, $\bar{u}_\xi(\xi)$, and the vapour pressure distribution. In this procedure, the thickness of the vapour layer ($\delta(\xi)$) and the extent of the layer (ξ_b), are obtained by a vapour-layer identification scheme based on the particle and droplet level set functions. Figure 5 illustrates the details of the scheme.

At every time step, a series of grid points near the particle surface are first identified to quantify the vapour layer. As shown in figure 5, these grids points are in a small band around the surface and can be outside the surface ($\ldots, i-1, i, i+1, i+2, \ldots$) or inside the surface ($\ldots, i'-1, i', i'+1, i'+2, \ldots$). If the droplet surface is represented by points ($\ldots, P_{i-1}, P_i, P_{i+1}, \ldots$) in figure 5 and point P_i is located on the mesh line between the mesh knots i and i', the vapour-layer thickness at P_i can be calculated based on the values of the level-set function at i and i', defined as $(\phi_{d,i}, \phi_{p,i})$ and $(\phi_{d,i'}, \phi_{p,i'})$, respectively. Since the level-set function is the signed distance from the computation knots to the droplet and particle surface after the redistance process is performed, the vapour-layer thickness (δ_i) at P_i can be estimated by:

$$\delta_i = \frac{\phi_{d,i} + \phi_{p,i} + \phi_{d,i'} + \phi_{\cdot p,i'}}{2} \tag{27}$$

The $u_{\lambda\delta}(\xi)$ is calculated by:

$$u_{\lambda\delta}(\xi) = \dot{m}/\rho_v - \frac{\partial\delta(\xi)}{\partial t}, \tag{28}$$

where the local evaporation rate $\dot{m}$ is defined by the heat transfer model. The vapour pressure force simulated by this model is applied as an interface force exerted on the computational cells on the bottom surface of the droplet.

4.4. *Heat transfer model*

The heat transfer model is applied to calculate the temperature distribution inside the particle and in the gas phase. Inside the particle, the heat conduction equation is given by:

$$\frac{\partial T_s}{\partial t} = \alpha_s \nabla \cdot \nabla T_s, \tag{29}$$

where α_s is the thermal diffusivity of the particle. When the particle surface is in contact with the droplet through the vapour layer, the boundary condition at the particle surface is given by:

$$k_v \frac{T_{p,surface} - T_{d,surface}}{\delta} = -k_s \boldsymbol{n}_p \cdot \nabla_p T_s \tag{30}$$

where $T_{p,surafce}$, $T_{d,surface}$ are the surface temperatures of the particle and the droplet, respectively; k_v, k_s are the heat conductivity of the vapour phase and the solid particle, respectively; $\boldsymbol{n}_p$ is the normal vector of the particle surface, $\nabla_p T_s$ is the temperature gradient which is evaluated only on the particle side. Similarly to the velocity interpolation at the particle surface discussed in § 4.2, this boundary condition, (30), is imposed on the computational grid point, which is located in a small band (2ε) near the particle surface on the solid side (figure 3). The temperatures defined at such grids are recalculated at each time step based on the temperature at the neighbouring grid points to satisfy the boundary condition given by (30).

Since the vapour layer is very thin, the temperature distribution in the vapour phase can be simplified to a one-dimensional equation in boundary-layer coordinates (Harvie & Fletcher 2001*a*, *b*):

$$\frac{\partial^2 T_v}{\partial \eta^2} = 0. \tag{31}$$

The radiative heat transfer across the vapour layer is neglected when the solid temperature is lower than 700 °C (Harvie & Fletcher 2001). Neglecting the radiative heat transfer across the vapour layer, the energy balance equation on the liquid–vapour interface can be given as:

$$k_v \frac{T_{ps} - T_{ds}}{\delta} = -k_d \frac{\partial T_d}{\partial \eta} + \dot{m} L_c, \tag{32}$$

where k_d is the thermal conductivity of the liquid droplet.

5. Results and discussion

Droplet–particle collision conditions under which experiments are conducted are simulated in this study. In the experiments, acetone droplets with 1.6–2.2 mm diameter impact on brass particles of 5.5 mm or 3.2 mm with $We = 3 \sim 20$. Initially, the droplet is at the saturation temperature (boiling point) of acetone. The particle temperature is 200°–300 °C, which is much higher than the boiling point of acetone, ensuring the non-wetting contact.

The simulation is conducted on uniform Cartesian meshes ($\Delta x = \Delta y = \Delta z = \Delta$). The advantage of using the uniform Cartesian mesh is that it can be generated easily and uses computational resources efficiently. Another benefit is that the computation code can be easily written without requiring an extra cell-index system. There are several reasons for not using the axisymmetric cylindrical meshes in this study.

Besides the complexity, the control volume scheme used in this study requires that each computation cell be a hexahedron. In the cylindrical coordinate, it is difficult to arrange the cells near the symmetrical axis to satisfy this condition. Moreover, the simulation code is developed to be capable of modelling various three-dimensional collision cases, such as the oblique collision shown in figure 19. In such cases, the flow field does not have any symmetrical axis, which make the axisymmetric mesh unsuitable for such three-dimensional simulation.

The time steps (Δt) are determined by the CFL (Courant–Friedrichs–Levy) condition and other conditions including the constraints of viscous and surface tension (Sussman, Smereka & Osher 1994). Other adjustable factors are the time step factor (0–1) and the under-relaxation factors. With $\Delta = 0.005\,\text{cm}$ and $80 \times 80 \times 100$ grid points, it takes 20–24 h for the Cray-X1 supercomputer at the Ohio Supercomputer Centre (OSC) to complete a typical droplet impact case in a real-time of 15–2 ms.

The experimental video frames and the simulated images (under each one) shown in figure 6 describe the impact of a saturated (56 °C) acetone droplet of 2.1 mm in diameter on a 5.5 mm particle at 250 °C. The impact velocity is $45\,\text{cm}\,\text{s}^{-1}$, which gives a Weber number of 12. The video frames were taken using a high-speed camera. The mesh resolution of the simulation shown in figure 6 is 0.06 mm in grid size, which gives a CPR (cell per droplet-radius) of 17.5. Other mesh sizes are also used to simulate the same impact case with comparisons of the results shown in figures 9 and 10.

In figure 6, the simulated three-dimensional images of the droplet and particle are presented which show the iso-value surface at the position with zero droplet and particle level set functions. The time indicated in the figure starts at the instant of the collision. The figure shows that the droplet shape variations in the video frames at various times are reproduced well by the simulation throughout the entire collision process. The droplet undergoes spreading, recoiling and rebounding during the contact. For both the experiments and the simulation, the results show that during the first 5.5 ms of the impact (0–5.5 ms), a liquid film with a flattened disk shape is formed immediately after the collision. The liquid film then spreads out on the particle surface. This stage of droplet spreading is caused by the inertial force which drives the liquid to flow out on the particle surface, until all the kinetic energy of the impact is either converted to the surface energy of the deformed droplet or dissipated by friction. The droplet film spreads to the maximum extent in about 7.5 ms (frame 4), yielding a radius of droplet–particle contact area about 1.5 times that of the original radius of the droplet. The liquid film then starts to shrink back to its centre (7.5–11.5 ms) owing to the surface tension force at the edge of the film. Beyond 11.5 ms, the liquid film continues to recoil and forms an upward jet in the centre of the droplet (11.5–17.5 ms), leading to the bouncing of the droplet up from the particle surface (21.5–27.5 ms). The peanut-shape droplet shown in the video frame at 21.5 ms is reproduced in the simulation.

The simulated cross-sectional images with velocity vectors of the droplet–particle collision are shown in figure 7. The droplet and particle images are generated by plotting the contour lines at the position with zero level set function. When the droplet initially approaches the solid surface, the bottom surface of the droplet is first flattened by the vapour pressure (0–1.5 ms). Frame 2 shows that the spreading speed of the liquid film is close to the initial impact velocity of the droplet. As the droplet continues to spread on the particle surface, the fluid mass starts to accumulate at the leading edge of the liquid film (5.5 ms). The velocity field in the image at 8.8 ms indicates that the inward flow starts from the outer edge of the liquid film, which

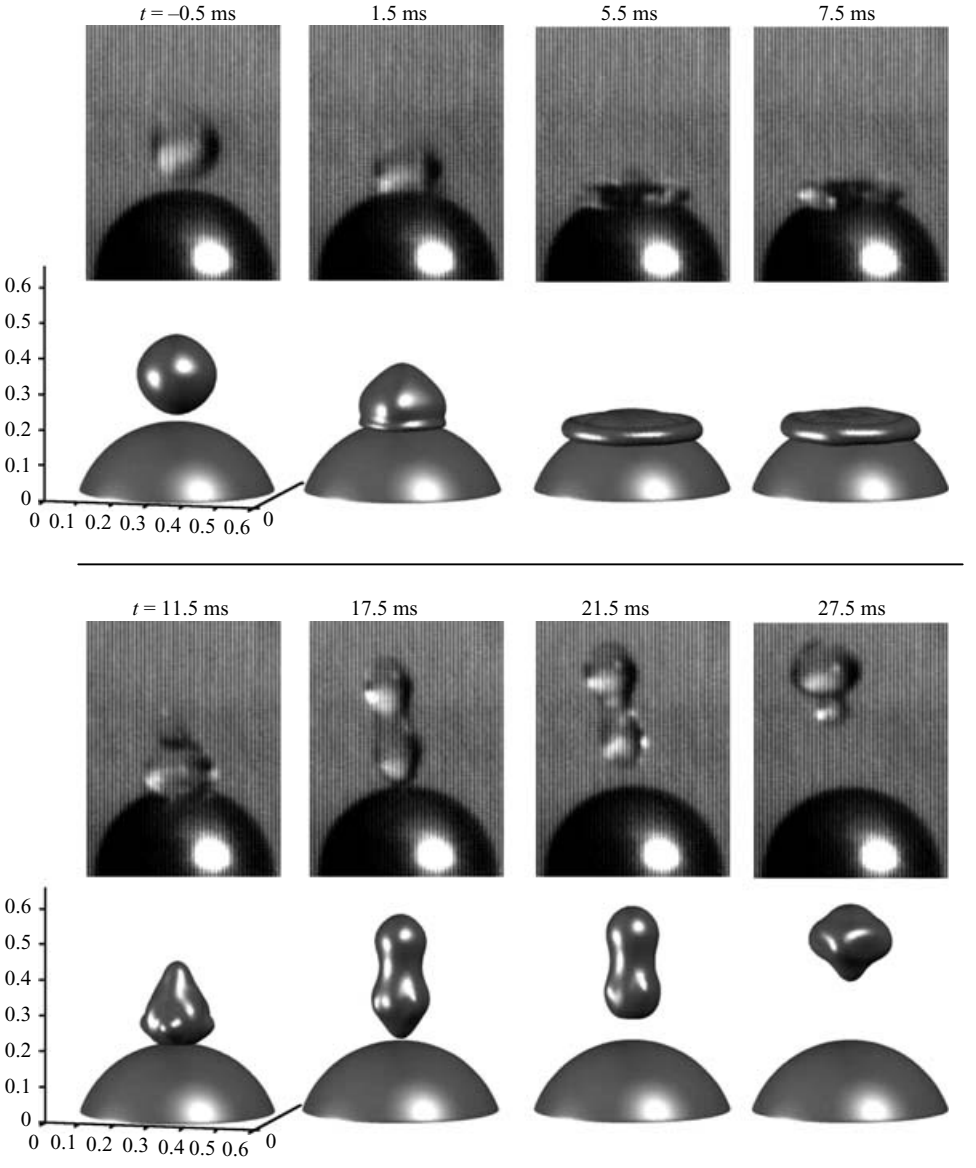

FIGURE 6. Experimental video frames and simulated images of the 2.1 mm acetone droplet impact on the 5.5 mm particle at 250 °C. The impact velocity is 45 cm s^{-1}, and $We = 12$. The unit for the coordinates is cm.

confirms that the recoiling flow is driven by the surface tension. The vapour layer between the droplet bottom surface and the particle surface is roughly visible during the recoiling process (8.8–11.0 ms). At 17.2 ms after the collision, the droplet rebounds away from the particle, and the droplet contact with the particle ceases.

The droplet dynamics during the collision can be described quantitatively by two parameters: the spread factor (r_c/r_0) and the dimensionless heights of the centre of gravity (H_c/r_0). The term r_0 is the initial radius of the droplet; r_c is the radius of the contact area of the droplet with the solid surface. The r_c and H_c are defined in figure 8.

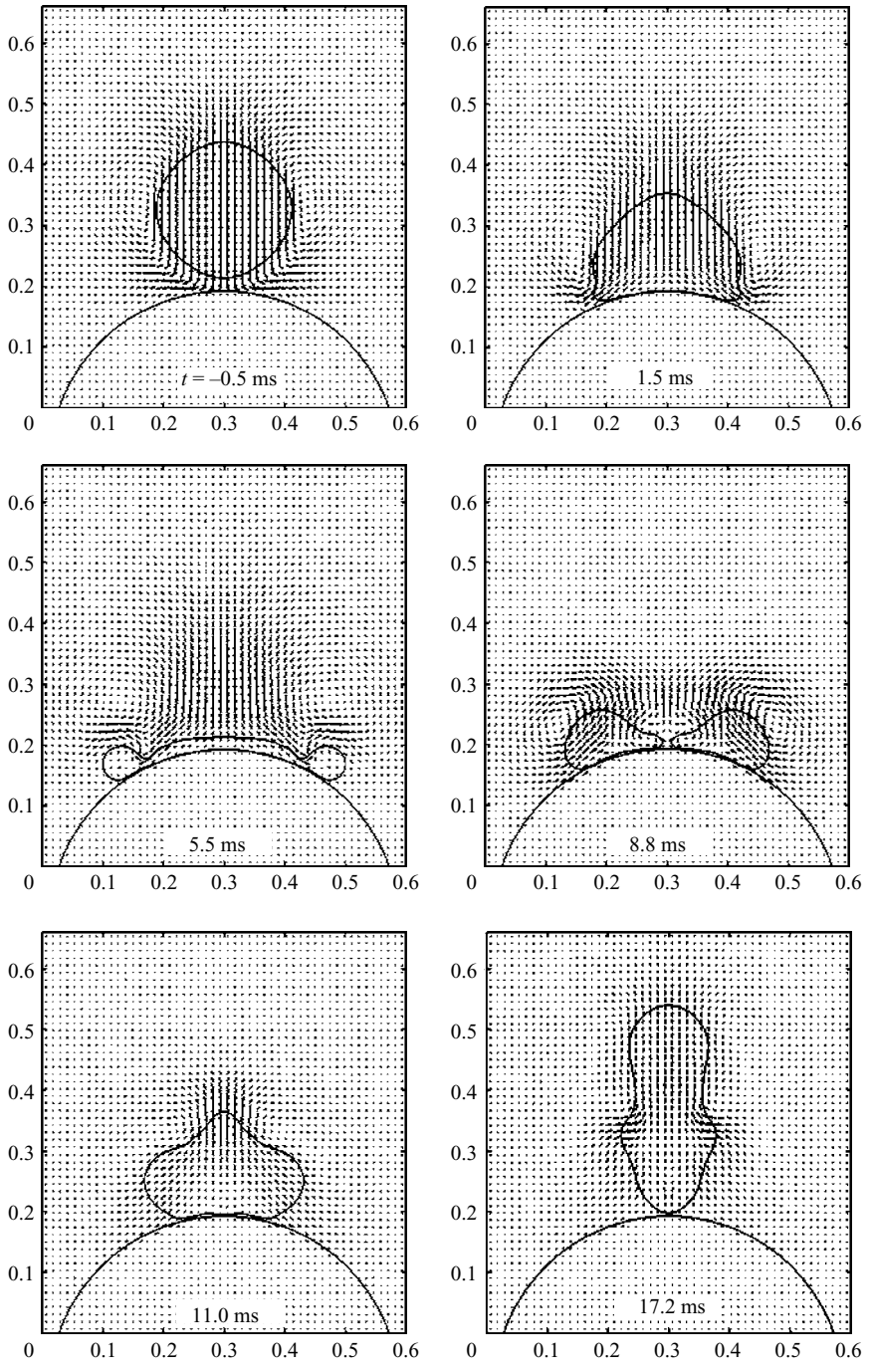

FIGURE 7. A simulated cross-sectional velocity field for the impact given in figure 6. The unit for the coordinates is cm.

In the simulation, the height of the centre of gravity is obtained by:

$$H_c = \frac{\sum\limits_{\phi<1.5\Delta} d_i \rho_i}{\sum\limits_{\phi<1.5\Delta} \rho_i}, \tag{33}$$

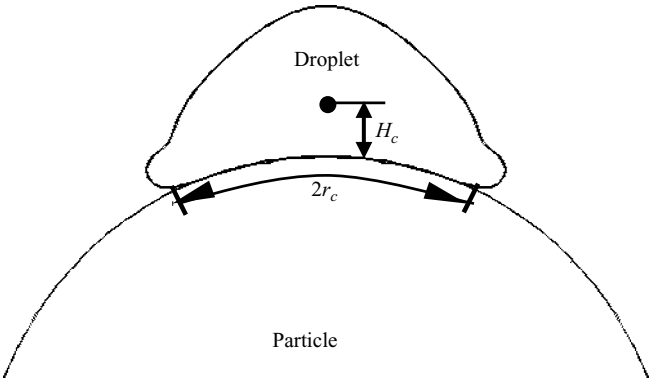

FIGURE 8. The definition of the spread factor and droplet height of the centre of gravity.

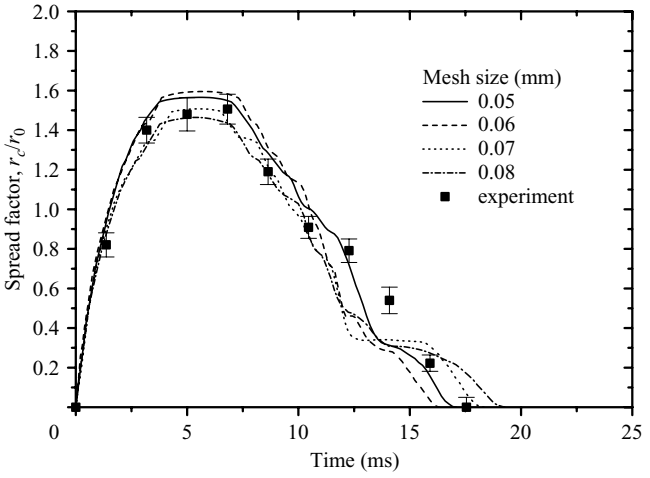

FIGURE 9. The simulated spread factor of the droplets during the impact shown in figure 6 at different mesh sizes.

where d_i is the distance between cell i and the particle surface, which is equal to the particle level-set function (ϕ_p); ρ_i is the density of the fluid in cell i.

In order to test the effects of the mesh size on the simulation results, the droplet–particle collision process shown in figures 6 and 7 is simulated for four different mesh sizes including 0.08, 0.07, 0.06 and 0.05 mm. The corresponding CPRs (cells per droplet radius) for these mesh sizes are 13.2, 15, 17.5 and 21.0, respectively. The quantitative comparisons of the simulation and measurement results are given in figures 9 and 10.

The simulated spread factors for different meshes are shown in figure 9 with the experimental values. The experimental data are taken based on the results from the video frames in figure 6. The general agreement between the experiments and the simulations for these mesh sizes is good. The effect of the mesh sizes on the spread factor is not significant before 2 ms, and becomes notable after 2 ms. The peak on the spread factor is seen to occur at 4.0–6.0 ms, corresponding to the maximum extent of the droplet spreading on the surface. The simulated contact time of the droplet–particle is around 16–18 ms, which is close to the experimental results and the first-order vibration period of the oscillating drop (Ge & Fan 2005).

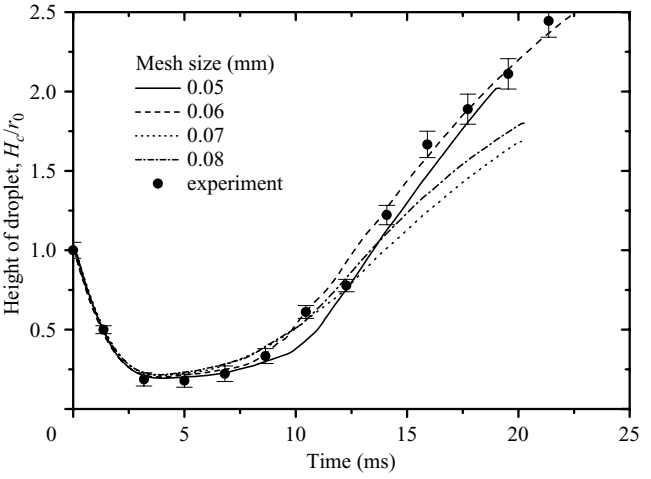

FIGURE 10. The simulated height of the centre of gravity of the droplets during the impact shown in figure 6 for different mesh sizes.

Figure 10 shows the dimensionless height of the centre of gravity of the droplet simulated at different mesh sizes. All curves reach their minimum at about 4.0–6.0 ms, corresponding to the time when the droplets have spread to their maximum extent on the surface. It can be seen that the mesh size in the simulation affects only the recoiling process, and the simulation on a coarser mesh (0.07 and 0.08 mm grid size) gives a lower height during the rebounding of the droplet. The agreement between the experimental and the simulation results with smaller mesh size (0.05 and 0.06 mm meshes) is good for the entire collision process.

In addition to droplet dynamics, the thermodynamic aspects of the particle–droplet collision are also important to account for the droplet evaporation process. The simulated temperature distribution inside the particle during the process of droplet–particle collision is shown in figure 11. The temperature variations on the particle surface and inside the particle at four different locations are shown in figure 12. The measured particle surface temperature in the experiments is also shown in figure 12. Recognizing that the thermocouple response time is 2 ms, the early part of the measured temperature curve, where the surface temperature is most likely to change very rapidly, might be attenuated. The simulated total heat transfer rate and average heat flux on the particle surface are shown in figure 13. The thickness and shape of the vapour layer between the droplet and particle is found to be similar to that for the droplet impact on the flat surface, which was described in Ge & Fan (2005, 2006).

The temperature field in the cross-section of the particle is shown in figure 11 for the droplet–particle collision conditions given in figures 6 and 7. The initial temperature of the particle is 250 °C. Immediately after the first droplet–particle contact (1.5 ms), the temperature drop inside the particle occurs at the contact area around the impact centre (point o in figure 4). With the spreading of the droplet on the particle surface (frames 1 to 2), the extent of the temperature drop inside the particle increases, but the position with a maximum temperature drop is sustained at the centre of the contact area (frames 1 to 4). The maximum temperature drop on the particle surface can reach ~20 °C which occurs at the end of the spreading stage of the droplet (5.5–8.8 ms). During the droplet recoiling process (8.8 ms–15.0 ms), the particle temperature near the droplet–particle contact area recovers from its earlier drop, which is caused

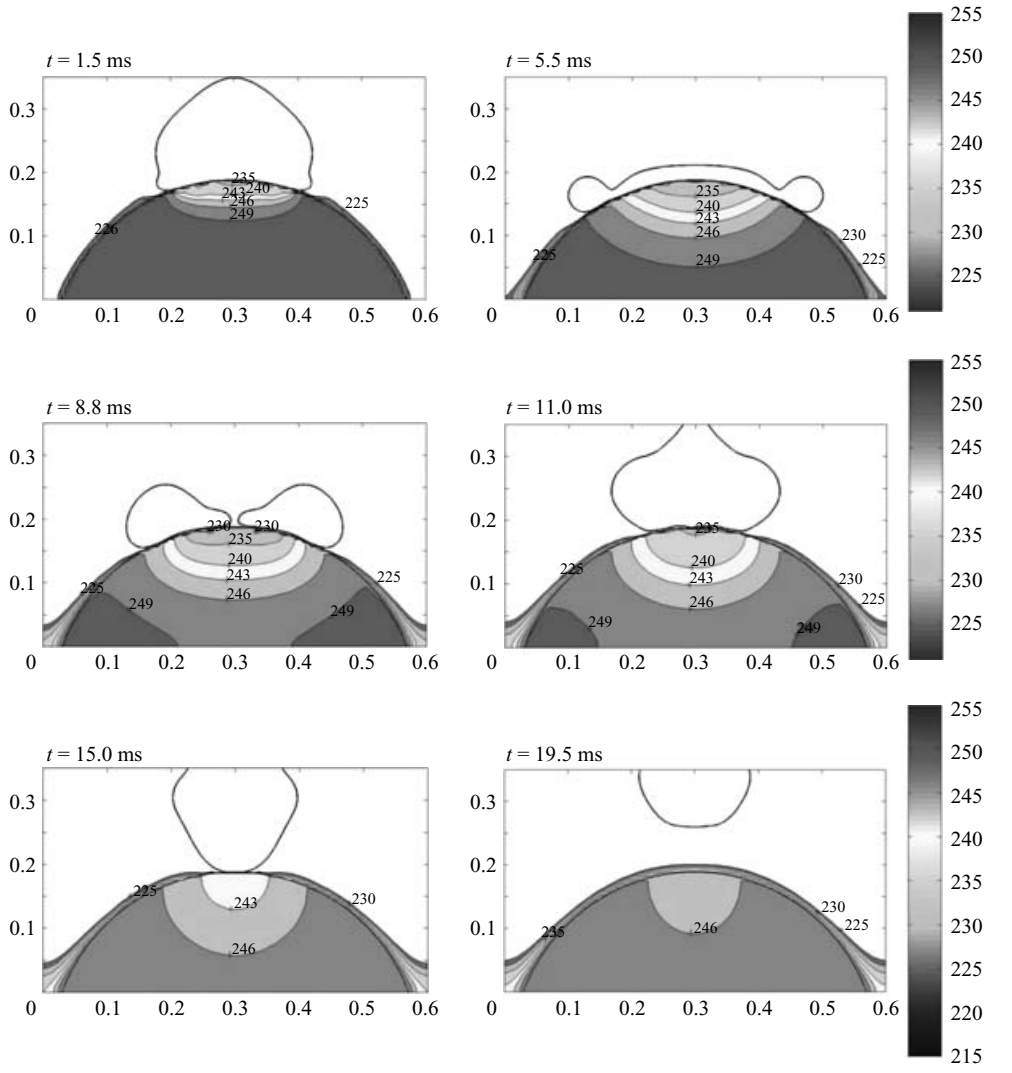

FIGURE 11. The simulated temperature field inside the particle for the impact shown in figure 6.

by the heat transfer from the bulk of the particle and the decreased heat transfer rate at the particle surface owing to the established vapour layer (also see figure 12). If the isotherm corresponding to 249 °C is chosen to represent the edge of the area undergoing the temperature drop during the impact, the extent of the particle affected by the droplet impact continues to grow toward the inner part of the particle throughout the entire collision process.

In figure 12, the simulated particle temperature at the centre of the droplet impact ($\xi = 0$) is compared with the experimental values. Four curves represent the temperatures at locations of different depths from the impact point on the surface with Z as the vertical coordinate. In the experiments, the particle temperature was measured by using a fast-response type T thermocouple inserted into the particle surface ($Z = 0$) from the bottom particle. Figure 12 shows that an abrupt temperature drop occurs on the particle surface immediately after the initial approach of the droplet

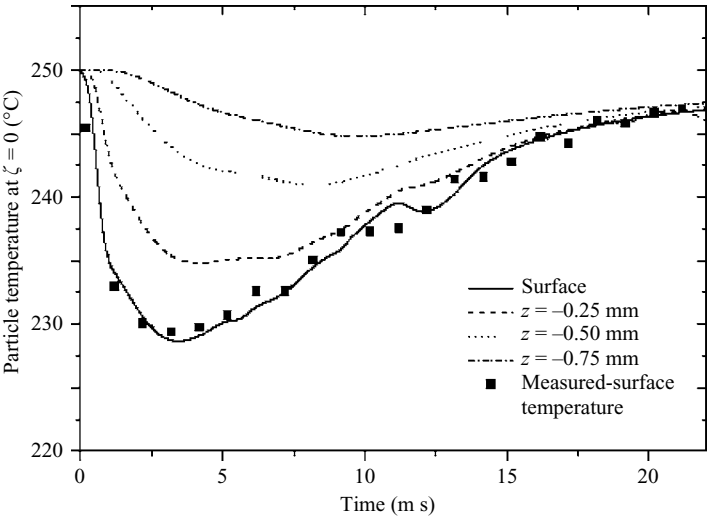

FIGURE 12. The particle temperature at $\xi = 0$ for different depths during the impact and comparisons with the experimental results.

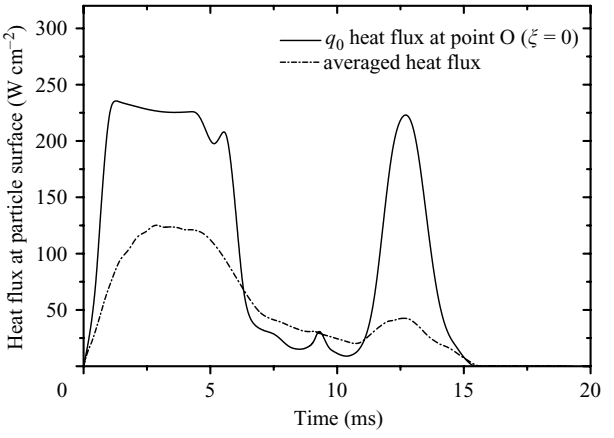

FIGURE 13. The simulated heat flux at the particle surface during the impact.

surface to the solid surface. The maximum temperature drop at the particle surface can reach ~22 °C, which occurs at 3–4 ms after the collision. The temperature then recovers at 5.5 ms, which corresponds to the transition time of the droplet movement from the spreading to the recoiling. The temperature drop becomes less significant at the location further beneath the surface. Although there exist small noises in the temperature measurement results, consistency in the temperature variation between the experimental results and the simulation results is reasonably good.

The transient heat flux at the centre of the contact area (q_o) and the averaged heat flux over the contact area ($\bar{q}$) on the particle surface are shown in figure 13. The heat flux q_o quickly reaches a level of 230 W cm^{-2} at 1.0–1.5 ms after the collision, and is sustained at this level until 6.5 ms, by which time the droplet film starts to recoil (see figure 6). The heat flux is relatively small during the droplet recoiling (6.5–11 ms), because the vapour layer is fully established during this period, hindering the heat transfer between the particle and the droplet. The second peak on the curve of q_o

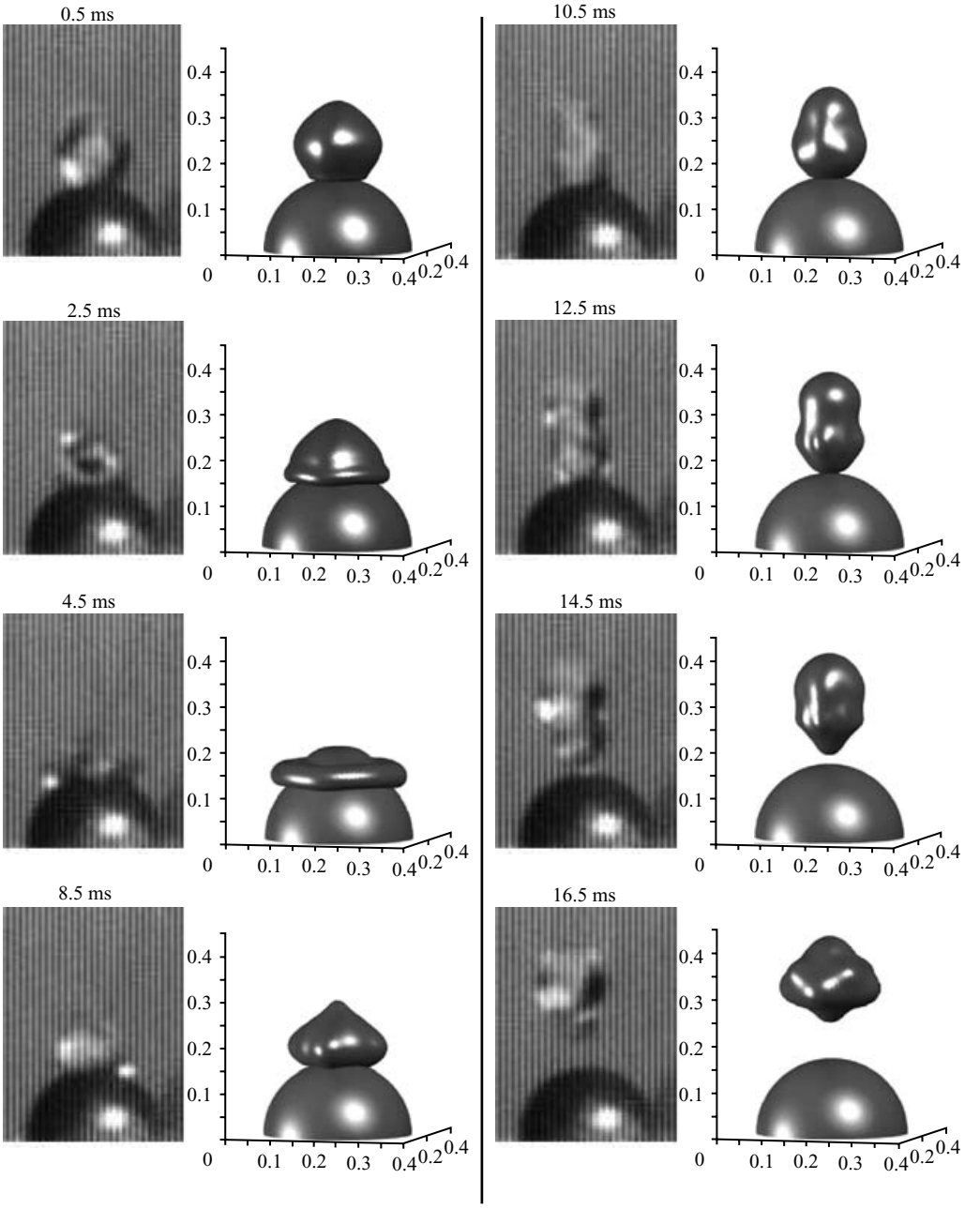

FIGURE 14. Experimental video frames and simulated images of the 1.8 mm acetone droplet impact on the 3.2 mm particle at 300 °C. The impact velocity is 40 cm s^{-1}, and $We = 8$.

at 13 ms corresponds to the close contact of the droplet bottom surface with the particle immediately before the droplet rebounds. The average heat flux $\bar{q}$ can reach 100 W cm^{-2} during the droplet spreading and can reduce to 30–40 W cm^{-2} during the droplet recoiling.

Both the simulation and experiments are performed for particles and droplets of different sizes. The collision process shown in figure 14 involves an acetone droplet of

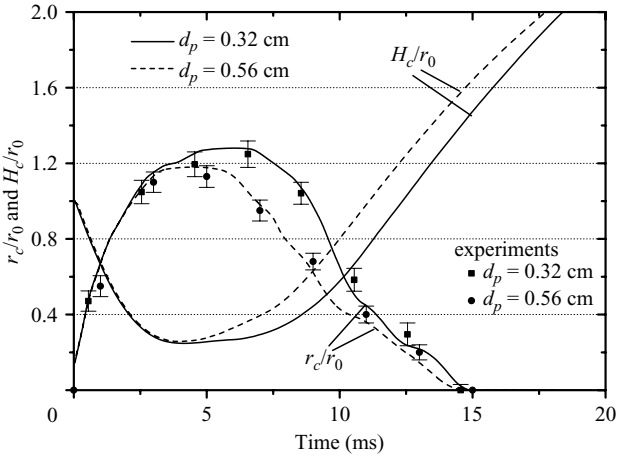

FIGURE 15. Simulated r_c/r_0 and H_c/r_0 for droplet impacts on the particles of different diameters and comparison with measured r/r_0.

1.8 mm in diameter and a brass particle of 3.2 mm in diameter at 300 °C. The collision velocity is 40 cm s^{-1}. The mesh size used in this simulation is 0.05 mm. Comparing the simulated results with the video frames, it can be seen that the entire process of droplet spreading, recoiling and rebounding is represented well by the simulation. In the spreading process (at 0–4.5 ms), the droplet expands along the particle surface and more fluid accumulates at the leading edge, forming a ring structure (4.5 ms). Compared to the collision case with a larger (5.5 mm) particle (figure 6), the liquid droplet can flow down and cover a larger fraction of the particle surface owing to a higher curvature of the small particle considered in this case. The recoiling of the droplet driven by the surface tension is less dramatic (4.5–10.5 ms), and the elongation of the droplet during the rebounding (10.5–16.5 ms) is smaller compared to the collision process shown in figure 6.

The dynamics of the droplet during its collision with particles of different sizes are examined. The spread factors (r_c/r_0) and the dimensionless heights of the centre of gravity of the droplet (H_c/r_0) for collisions with the particles of 3.2 mm and 5.5 mm in diameter are compared in figure 15. With other conditions identical to those given in figure 14, the simulation results indicate that during the early stage of the droplet spreading (0–4 ms), r_c and H_c are almost the same for both particles. Later, it can be seen that the droplet for the smaller particle spreads to a larger extent on the particle surface. Although the spread factors are different for collisions with two different particle sizes during the recoiling period, the contact times of the droplet with the surface of both particles are very similar ($\sim$14.5 ms), and can be estimated by the first-order vibration period of the droplet. The variations of H_c/r_0 in figure 15 also show that the droplet rebounds higher from a larger particle surface. The measured r_c/r_0 in the experiments from this study is also illustrated in figure 15, which confirms the trends obtained from the simulation.

The computation is further extended to analyse the effects of the collision velocity on the hydrodynamic and thermodynamic aspects of the collision process. The simulation is conducted for three cases with collision velocities of 25, 40 and 60 cm s^{-1}, corresponding to Weber numbers of 3, 8 and 18, respectively. In these cases, the particle size used is 5.5 mm and other conditions remain the same as those shown in figure 14. The simulation results are given in figures 16, 17 and 18.

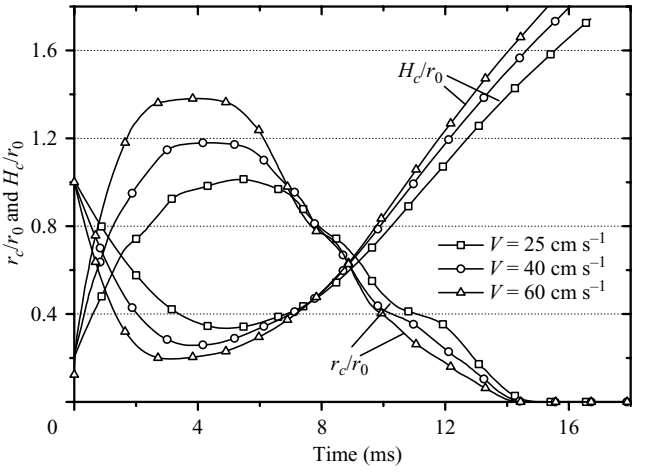

FIGURE 16. Simulated r_c/r_0 and H_c/r_0 for droplet impacts on the 5.5 mm particle with different impact velocities. The corresponding Weber numbers are 3, 8 and 18, respectively.

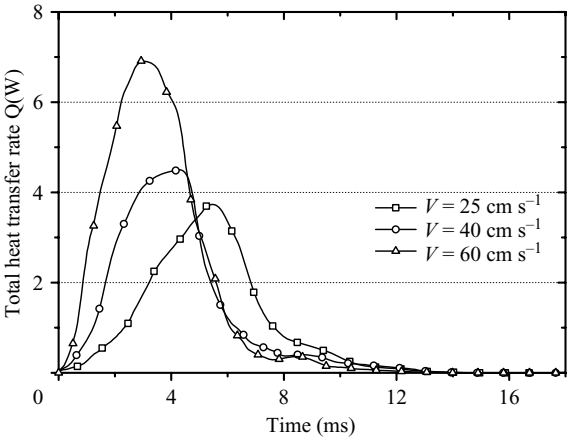

FIGURE 17. Simulated total heat transfer at the particle surface during the impact with different impact velocities.

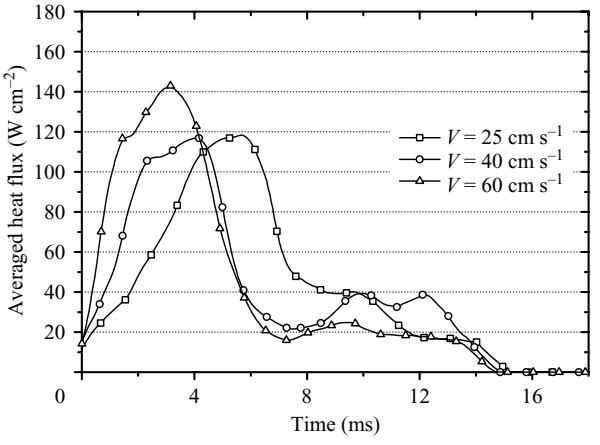

FIGURE 18. Averaged heat flux at the particle surface during the impact with different impact velocities.

The variations of r_c/r_0 and H_c/r_0 with time during the collision at different velocities are given in figure 16. The curves of H_c/r_0 show that the height of the centre of gravity of the droplet reaches its minimum at about 3.5–4.5 ms, corresponding to its time when the droplet spreads to its maximum extent on the particle surface. The impact at a larger impact velocity yields a lower height of centre of the gravity during the spread, but reaches a higher rebounding height.

It is also seen in figure 16 that for all three different velocities, r_c/r_0 reaches zero at $t \sim 14.5$ ms. The comparison of these curves indicates that although the maximum spread factor is larger for the impact with a higher impact velocity, the contact time appears to be independent of the impact velocity. Wachters & Westerling (1966) suggested that the contact time for a liquid droplet impact on a hot flat surface was independent of the impact velocity, and could be estimated by the first-order vibration period of the droplet as given by:

$$\tau = \pi R_d \sqrt{\frac{\rho_l R_d}{2\sigma}}. \tag{34}$$

The estimated contact time by (34) for this case is 13 ms, which is close to the simulated values for all three impact velocities (~14.5 ms). Richard, Clanet & Quéré (2002) studied the impact of a droplet on a super-hydrophobic surface under the isothermal condition, and found the contact time to be $\tau = \sqrt{\rho_l R_d^3/\sigma}$. The expression of the contact time has a similar form to that of Wachters & Westerling (1966); however, the contact time of Richard *et al.* is smaller than that of Wachters & Westerling by a factor of $\pi/\sqrt{2}$. Although both studies concern the non-wetting impact of a droplet on a surface, the non-wetting conditions for the surfaces are different. The non-wetting is provided by a vapour layer for the former and by the super-hydrophobicity of the surface for the latter. Evidently, the slip vapour-layer surface in the case of Wachters & Westerling (1966) would yield a wider spread area, hence a longer contact time, compared to the non-slip solid surface in the case of Richard *et al.* (2002). We have shown that for droplet impact on a hot particle whose size is comparable to the droplet, the estimation for the contact time in Wachters & Westerling (1966) is still applicable.

The effect of the collision velocity on the heat transfer at the particle surface is illustrated in figures 17 and 18. The total heat transfer rate (Q) at the particle surface for three collision velocities is shown figure 17. The value for Q is calculated by integrating the heat flux across the contact area of the droplet and the particle. It is found that the collision with a higher relative velocity gives a higher heat loss of the particle because the higher collision velocity yields a larger spreading extent (figure 16). Most (80 %–90 %) of the heat loss of the particle takes place during the period of the first 6–7 ms of the impact, for a total contact time of 14–15 ms. The larger contact area in the spreading process is the reason for the higher heat transfer rate in this period. Based on the total heat transfer rate (Q) shown in figure 17, the total heat transferred between the droplet and the particle during the collision can be calculated. For three cases with collision velocities of 25, 40 and 60 cm s^{-1}, the total heat transferred is of 0.16 J, 0.018 J and 0.022 J, respectively. Assuming all of this heat energy is consumed by the liquid evaporation, the vaporized liquid mass is of 0.0162 mg, 0.0182 mg and 0.0223 mg, which are equivalent to, respectively, 0.42 %, 0.48 % and 0.59 % of the total droplet mass.

The averaged heat fluxes ($\bar{q}$) over the contact area during the collisions for three impact velocities are compared in figure 18. It is noted that the $\bar{q}$ curve for a higher

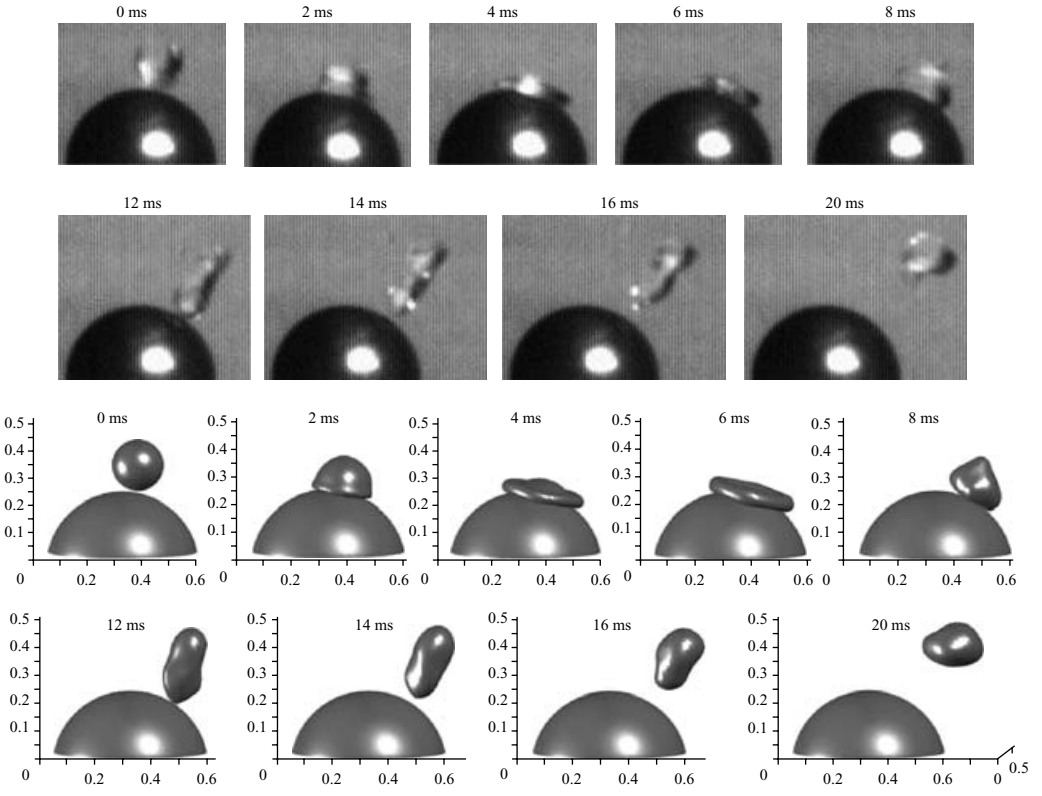

FIGURE 19. Experimental video frames and simulated three-dimensional images of the oblique collision of the 1.9 mm acetone droplet with the 5.6 mm brass particle.

collision velocity has an earlier peak. Relatively, the peak value for the heat flux curve is less dependent on the collision velocities. For three collision velocities, the heat fluxes first reach a higher level during the spreading process, then sharply decrease and gradually level off at a later stage of the recoiling process.

Considering an oblique collision between a droplet and a particle, there is no axis of symmetry for the flow. In this case, only the three-dimensional model is capable of carrying out the simulation. Figure 19 shows both simulated three-dimensional results and experimental video frames of an oblique collision between a 1.9 mm acetone droplet and a 5.5 mm brass particle at a velocity of $40\,\mathrm{cm\,s^{-1}}$. The initial temperature of particle is 300 °C. The offset of the centres of the droplet and the particle is 0.4 mm. The cross-sectional images with the simulated temperature field of this oblique collision are given in figure 20. The simulation is run on a $160 \times 120 \times 100$ mesh, which gives a mesh size of 0.05 mm.

Comparing the simulation with the experimental results, it can be seen that the droplet dynamics, including the evolution of its shapes, are reproduced well by the computation. In the first 4.0 ms of the impact (frames 1 to 3), the droplet spreads out immediately after the contact, in a manner similar to the normal collision, and the location of the centre of the disk-like liquid film shifts along the particle surface away from the initial contact point. When the droplet reaches the maximum diameter at 6.0 ms, the liquid film starts to retreat back to its centre (frames 4 to 6) owing to the surface tension force induced from the periphery of the droplet. During this process,

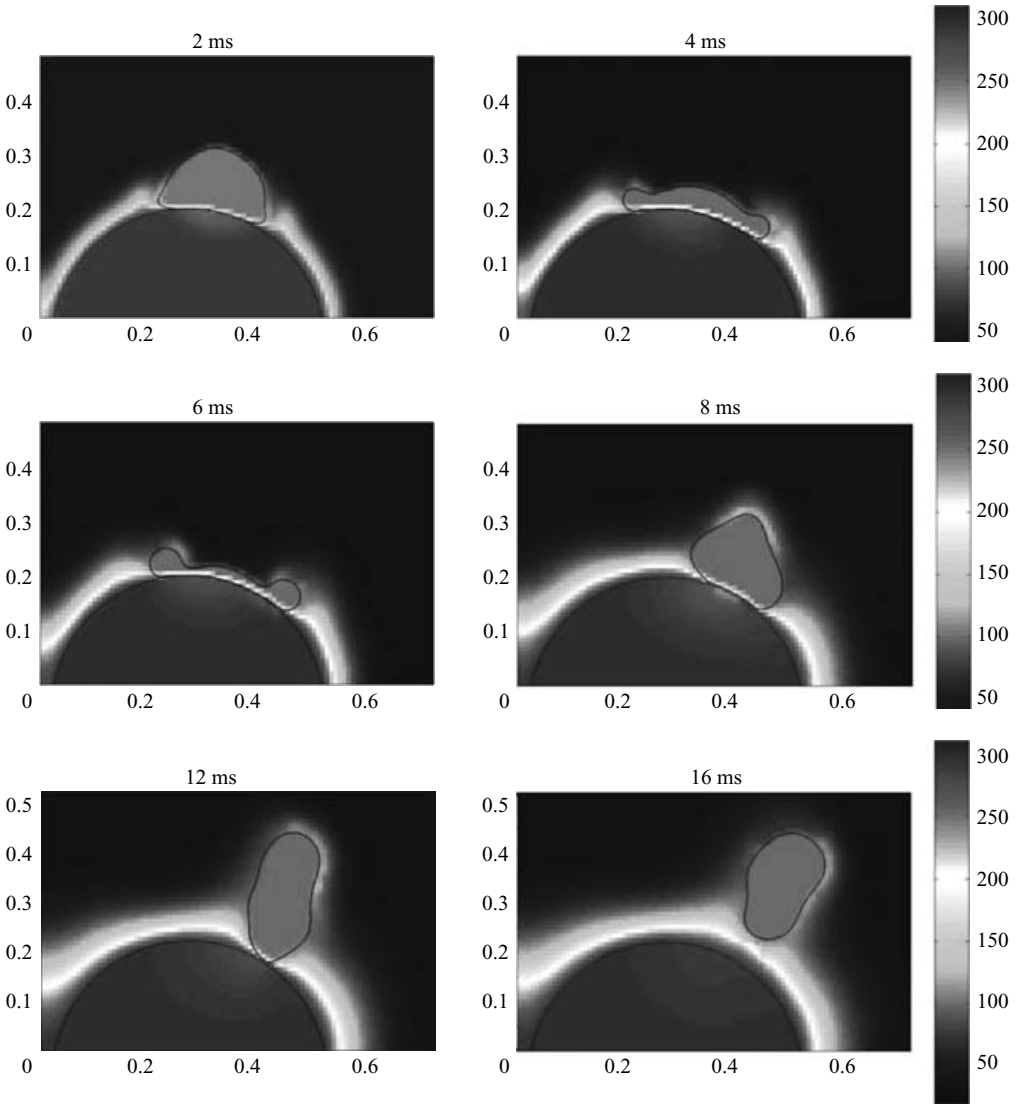

FIGURE 20. Simulated temperature fields during the oblique impact process shown in figure 19.

the droplet continues slipping on the particle surface. After the droplet rebounds from the particle surface (frames 7 to 9), the displacement of the droplet from its initial collision position is significant, even if the offset is very small (0.4 mm) at the beginning. This can be considered as evidence of the indirect contact of the liquid and solid under the film boiling condition, which gives a free-slip boundary condition on the particle surface.

Figure 20 shows the calculated temperature distributions for the collision process shown in figure 19. During the entire process, the bulk of the liquid droplet remains at its saturated temperature. Inside the particle, the temperature drop occurs near the contact area. As the liquid film shifts on the particle surface, the location with the maximum temperature drop inside the particle also shifts with the contact area.

6. Conclusions

The three-dimensional computational model developed in this study is capable of reproducing the droplet–particle collision process with significant heat transfer and phase change (evaporation). The level-set method and the immersed-boundary method are combined to describe the droplet–particle contact dynamics in the fixed Eulerian grid. The heat transfer properties in each phase are solved with a micro-scale vapour flow model which is applied to determine the vapour pressure force during the contact process between the droplet and the superheated particle. Droplet collision with the smaller particle spreads to a larger extent on the particle surface, but rebounds higher from a larger particle surface. Although a larger impact velocity gives a larger spreading extent, the contact time of the droplet on the particle surface is almost independent of the impact velocity. The heat flux on the particle surface reaches a higher level during the spreading process, and then sharply decreases during the recoiling process. In the oblique collision, the displacement of the droplet from its initial collision position is significant, even though the offset of the centres of the droplet and the particle is very small at the beginning of the droplet–particle contact.

The assistance of Dr Raymond Lau in the experimental work and Mr Zhao Yu in the manuscript revision is gratefully acknowledged. The work was supported in part by the Ohio Supercomputer Centre.

REFERENCES

Brackbill, J. U., Kothe, D. B. & Zemach, C. 1992 A continuum method for modeling surface tension. *J. Comput. Phys.* **100**, 335–354.

Bussmann, M., Mostaghimi, J. & Chandra, S. 1999 On a three-dimensional volume tracking model of droplet impact. *Phys. Fluids* **11**, 1406–1417.

Bussmann, M., Mostaghimi, J. & Chandra, S. 2000 Modeling the splash of a droplet impacting a solid surface. *Phys. Fluids* **12**, 3121–3132.

Chandra, S. & Avedisian, C. T. 1991 On the collision of a droplet with a solid surface. *Proc. R. Soc. Lond.* A **432**, 13–41.

Chen, C. & Fan, L.-S. 2004 Discrete simulation of gas–liquid bubble column and gas–liquid–solid fluidized bed. *AIChE J.* **50**, 288–301.

Chen, J. C. & Hsu, K. K. 1995 Heat transfer during liquid contact on superheated surfaces. *J. Heat Transfer* **117**, 693–697.

Chizhov, A. V. & Takayama, K. 2004 The impact of compressible liquid droplet on hot rigid surface. *Intl J. Heat Mass Transfer* **47**, 1391–1401.

Fadlun, E. A., Verzicco, R., Orlandi, P. & Yusof, J. M. 2000 Combined immersed-boundary finite-difference methods for three-dimensional complex flow simulations. *J. Comput. Phys.* **161**, 35–60.

Fan, L.-S., Lau, R., Zhu, C., Vuong, K., Warsito, W., Wang, X. & Liu, G. 2001 Evaporative liquid jets in gas–liquid–solid flow system. *Chem. Engng Sci.* **56**, 5871–5891.

Francois, M. & Shyy, W. 2003 Computations of drop dynamics with the immersed boundary method. Part 1: numerical algorithm and buoyancy-induced effect. *Numer. Heat Transfer* B **44**, 101–117.

Fujimoto, H. & Hatta, N. 1996 Deformation and rebounding processes of a water droplet impinging on a flat surface above Leidenfrost temperature. *Trans. ASME* I: *J. Fluids Engng* **118**, 142–149.

Fukai, J., Shiiba, Y., Yamamoto, T. & Miyatake, O. 1995 Wetting effects on the spreading of a liquid droplet colliding with a flat surface: experiment and modeling. *Phys. Fluids* **7**, 236.

Ge, Y. & Fan, L.-S. 2005 Three-dimensional simulation of impingement of a liquid droplet on a flat surface in the Leidenfrost regime. *Phy. Fluids* **17**, 027104.

Ge, Y. & Fan, L.-S. 2006 3-D modeling of the dynamics and heat transfer characteristics of a sub-cooled droplet impact on a superheated flat surface. *Intl J. Heat Mass Transfer* **49**, 4231–4249.

Goldstein, D., Handler, R. & Sirovich, L. 1993 Modeling a no-slip flow boundary with an external force field. *J. Comput. Phys.* **105**, 354.

Gottfried, B. S., Lee, C. J. & Bell, K. J. 1966 The Leidenfrost phenomenon: film boiling of liquid droplets on a flat plate. *Intl J. Heat Mass Transfer* **9**, 1167–1187.

Harlow, F. H. & Shannon, J. P. 1967 The splash of a liquid droplet. *J. Appl. Phys.* **38**, 3855.

Harvie, D. J. E. & Fletcher, D. F. 2001*a* A hydrodynamic and thermodynamic simulation of droplet impacts on hot surface. Part I, theoretical model. *Intl J. Heat Mass Transfer* **44**, 2633–2642.

Harvie, D. J. E. & Fletcher, D. F. 2001*b* A hydrodynamic and thermodynamic simulation of droplet impacts on hot surface. Part II, validation and applications. *Intl J. Heat Mass Transfer* **44**, 2643–2659.

Hatta, N., Fujimoto, H., Kinoshita, K. & Takuda, H. 1997 Experimental study of deformation mechanism of a water droplet impinging on hot metallic surface above the Leidenfrost temperature. *Trans. ASME* I: *J. Fluids Engng* **119**, 692–699.

Inada, S., Miyasaka, Y. & Nishida, K. 1985 Transient heat transfer for a water drop impinging on a heated surface. *Bull. JSME* **28**, 2675–2681.

Kashiwa, B. A., Padial, N. T., Rauenzahn, R. M. & Vanderheyden, W. B. 1994 A cell-centered ICE method for multiphase flow simulation. *Los Alamos National Laboratory Res. Rep.* LA-UR-93-3922.

Karl, A., Anders, K., Rieber, M. & Frohn, A. 1996 Deformation of liquid droplets during collisions with hot walls: experimental and numerical results. *Part. Part. Syst. Charact.* **13**, 186–191.

Mehdi-Nejad, V., Mostaghimi, J. & Chandra, S. 2003 Air bubble entrapment under an impacting droplet. *Phys. Fluids* **15**, 173–183.

Osher, S. & Sethian, J. A. 1988 Fronts propagation with curvature-dependent speed: algorithms based on Hamilton–Jacobi formulation. *J. Comput. Phys.* **79**, 12.

Pasandideh-Ford, M., Bhola, R., Chandra, S. & Mostaghimi, J. 1998 Deposition of tin droplets on a steel plate: simulation and experiments. *Intl J. Heat Mass Transfer* **41**, 2929–2945.

Peskin, C. S. 1977 Numerical analysis of blood flow in the heart. *J. Comput. Phys.* **25**, 220.

Qiao, Y. M. & Chandra, S. 1996 Boiling of droplet on a hot surface in low gravity. *Intl J. Heat Mass Transfer* **39**(7), 1379–1393.

Richard, D., Clanet, C. & Quéré, D. 2002 Contact time of a bouncing drop. *Nature* **417**, 811.

Sussman, M., Smereka, P. & Osher, S. 1994 A level set approach for computing solutions to incompressible two-phase flow. *J. Comput. Phys.* **114**, 146–159.

Sussman, M., Fatemi, E., Smereka, P. & Osher, S. 1998 An improved level set method for incompressible two-phase flows. *Comput. Fluids* **27**, 663–680.

Wachters, L. H. J. & Westerling, N. A. J. 1966 The heat transfer from a hot wall to impinging water drops in the spheroidal state. *Chem. Engng Sci.* **21**, 1047–1056.

Wachters, L. H. J., Bonne, H. & Nouhuis, H. J. 1966 The heat transfer from a hot horizontal plate to sessile water drops in the spheroidal state. *Chem. Engng Sci.* **21**, 923–936.

Zheng, L. L. & Zhang, H. 2000 An adaptive level set method for moving-boundary problem: application to droplet spreading and solidification. *Numer. Heat Transfer* B **37**, 437–454.

Zhu, C., Wang, X. & Fan, L.-S. 2000 Effect of solids concentration on evaporative liquid jets in gas-solid flows. *Powder Technology* **111**, 79–82.